Physica Medica 70 (2020) 109–117

Contents lists available at ScienceDirect

Physica Medica

journal homepage: www.elsevier.com/locate/ejmp

Original paper

Simulation of hypoxia PET-tracer uptake in tumours: Dependence of clinical uptake-values on transport parameters and arterial input function

Isabela Paredes-Cisneros[a,b,c,*], Christian P. Karger[a,b], Paola Caprile[d], David Nolte[e,f], Ignacio Espinoza[d], Araceli Gago-Arias[d,g]

[a] German Cancer Research Center (DKFZ), Department of Medical Physics in Radiation Oncology, Heidelberg, Germany
[b] Heidelberg Institute for Radiation Oncology (HIRO), National Center for Radiation Research in Oncology (NCRO), Heidelberg, Germany
[c] Heidelberg University, Faculty of Physics and Astronomy, Heidelberg, Germany
[d] Pontificia Universidad Católica de Chile, Institute of Physics, Santiago, Chile
[e] Universidad de Chile, Center for Mathematical Modeling, Santiago, Chile
[f] University of Groningen, Johann Bernoulli Institute, Groningen, The Netherlands
[g] Instituto de Investigación Sanitaria de Santiago (IDIS), Group of Medical Physics and Biomathematics, Santiago de Compostela, Spain

ARTICLE INFO

Keywords:
Hypoxia tracer uptake
Positron-emission-tomography (PET)
Radiotherapy
Computer simulation

ABSTRACT

Poor radiotherapy outcome is in many cases related to hypoxia, due to the increased radioresistance of hypoxic tumour cells. Positron emission tomography may be used to non-invasively assess the oxygenation status of the tumour using hypoxia-specific radiotracers. Quantification and interpretation of these images remains challenging, since radiotracer binding and oxygen tension are not uniquely related. Computer simulation is a useful tool to improve the understanding of tracer dynamics and its relation to clinical uptake parameters currently used to quantify hypoxia. In this study, a model for simulating oxygen and radiotracer distribution in tumours was implemented to analyse the impact of physiological transport parameters and of the arterial input function (AIF) on: oxygenation histograms, time-activity curves, tracer binding and clinical uptake-values (tissue-to-blood ratio, TBR, and a composed hypoxia-perfusion metric, FHP). Results were obtained for parallel and orthogonal vessel architectures and for vascular fractions (VFs) of 1% and 3%. The most sensitive parameters were the AIF and the maximum binding rate (K_{max}). TBR allowed discriminating VF for different AIF, and FHP for different K_{max}, but neither TBR nor FHP were unbiased in all cases. Biases may especially occur in the comparison of TBR- or FHP-values between different tumours, where the relation between measured and actual AIF may vary. Thus, these parameters represent only surrogates rather than absolute measurements of hypoxia in tumours.

1. Introduction

Hypoxia is known to negatively impact radiotherapy outcome [1,2]. Positron emission tomography (PET) can be used to assess the hypoxic status of tumours, using a hypoxia-specific radiotracer [3,4]. PET-based assessment of hypoxia has been found to be of prognostic value [5–7], and targeting hypoxia is a powerful therapeutic strategy for the individualized treatment of cancer patients [8,9]. Previous studies have shown that tracer kinetics in PET, represented as time-activity curves (TACs), can provide valuable information, although often only the static signal (e.g. two hours after tracer injection) is used. However, none of these methods have reached the status of clinically accepted routine and assessment of tumour hypoxia still imposes a great challenge [10]. The main obstacle lies in the limited understanding of the radiotracer dynamics and its binding, which is heavily influenced by various physiological factors.

Mathematical modelling of the underlying processes of oxygenation and hypoxia [11–13], as well as of the hypoxia-PET tracer uptake distributions in tumours [14–23] provide a valuable tool to better understand the resulting PET signal.

The model developed by Mönnich *et al.* [17] allowed reproducing experimental TACs from patients, based on the current understanding on the involved microscopic processes. As for any model, input parameters must be provided and the obtained results therefore depend on such input. For radiotracer dynamics, input parameters modulate diffusion and binding in the tumour, as well as the delivery of the tracer from the vessels into the tumour. Of particular relevance is the arterial input function (AIF), which describes the delivery of the tracer into the

* Corresponding author at: Im Neuenheimer Feld 280, German Cancer Research Center (DKFZ), Department of Medical Physics in Radiation Oncology (E040), Applied Medical Radiation Physics (E040-2), 69120 Heidelberg, Germany.
E-mail address: i.paredescisneros@dkfz.de (I. Paredes-Cisneros).

https://doi.org/10.1016/j.ejmp.2020.01.012
Received 7 October 2019; Received in revised form 10 January 2020; Accepted 11 January 2020
Available online 29 January 2020

region of interest. The AIF is usually determined in a large vessel or in the heart, indicating that it might not be representative for the tissue of interest, e.g. the tumour.

The aim of this study is firstly to implement a model to simulate the oxygen and ^{18}F-fluoromisonidazole (FMISO) distributions in tissue and to analyse the sensitivity on several input parameters that may impact the FMISO uptake. In a second step, the impact of the most relevant parameters on clinical criteria used for PET-based hypoxia assessment is studied. Different oxygenation levels in the tumour are considered by using vascular fractions (VFs) of 1% and 3%, and the effect of vascular geometry variation is studied by random sampling of the vessel distribution. The parametric sensitivity study includes tracer diffusion and binding, necrosis in strongly hypoxic areas, as well as properties of the AIF. Results are represented in terms of oxygen histograms and TACs, and by analysing the relationship between bound tracer and oxygen concentrations. Additionally, the clinical parameter tissue-to-blood ratio (TBR) was calculated and compared with the hypoxia-perfusion compound parameter FHP proposed by Mönnich *et al.* [17].

2. Materials and methods

2.1. Mathematical models for oxygen and tracer transport

2.1.1. Partial oxygen pressure distribution in tumours

It is assumed that oxygen diffuses from vessels into tumour tissue, where it is consumed by cells. These two processes are described by a reaction-diffusion partial differential equation (PDE), as shown in previous studies [11,12,16,24]:

$$\frac{\partial P}{\partial t} = D_{O_2}\nabla^2 P - g_{max}\frac{P}{P + P_0} = 0 \tag{1}$$

If the derivative on the left side is set to zero, P describes the stationary spatial distribution of oxygen partial pressure defined in a cubic volume of tumour tissue (V). D_{O_2} is the oxygen diffusion coefficient and g_{max} is the maximum oxygen consumption rate. Oxygen consumption is modelled by the Michaelis-Menten relation (third term in Eq. (1)), in which P_0 is the Michaelis-Menten coefficient (partial oxygen pressure at which consumption is reduced to 50%). Oxygen diffusion through the vessel walls is described by the capillary permeability coefficient L_{O_2}, and the vessel-to-tissue concentration difference. This is included by the boundary condition at the vessel surface $\vec{n}\bullet(D_{O_2}\nabla P) = L_{O_2}(P_{iv} - P)$, where P_{iv} is the intravessel-value of Pin tumours.

2.1.2. Hypoxia-radiotracer dynamics

As for the oxygen, blood vessels are also the source of the FMISO radiotracer, which diffuses into the tissue and binds in hypoxic cells. The total tracer concentration is composed by a free and a bound term $C = C_f + C_b$, modelled by reaction-diffusion PDEs [16,17].

$$\frac{\partial C_f}{\partial t} = D_T\nabla^2 C_f - K(P)C_f \tag{2a}$$

$$\frac{\partial C_b}{\partial t} = K(P)C_f \tag{2b}$$

D_T is the FMISO diffusion coefficient and the oxygen-dependent irreversible tracer binding rate is described by the coefficient $K(P) = F_1(P)\bullet F_2(P)$. In this expression, F_1 considers a hyperbolic relation between binding rate and the oxygen concentration P[14]:

$$F_1 = K_{max}\frac{P_1}{P + P_1} \tag{3a}$$

K_{max} is the maximum binding rate and P_1 describes the oxygen partial pressure at which the binding rate amounts to 50% of its maximum. Assuming that cells at very low oxygen concentration become necrotic and lose their capability for tracer-uptake, the second term F_2 limits the binding according to:

$$F_2 = \left(\frac{P}{P + P_2}\right)^k \tag{3b}$$

Here, P_2 describes the oxygen concentration at which 50% of the cells become necrotic and k describes the steepness of this transition.

The tracer flow through the vessels walls depends on the capillary permeability for the tracer L_T, and the tissue-vessel tracer concentration difference, written as the boundary condition:

$$\vec{n}\bullet(D_T\nabla C_f) = L_T(\mathrm{AIF}(t) - C) \tag{4}$$

Through this boundary condition the AIF is introduced into the system: the AIF is the time-dependent tracer concentration of the tumour-supplying artery. As in a previous study by Wack *et al.* [21], the AIF was fitted by the double-exponential decay-function:

$$\mathrm{AIF}(t) = A_1 e^{-\tau_1 t} + A_2 e^{-\tau_2 t} \tag{5}$$

In Eq. (5), τ_1, τ_2, A_1, and A_2 are the fit parameters describing the tracer removal from the blood with two different rates (τ_1, τ_2) and their relative contributions (A_1, A_2), respectively.

Assuming similar tumour tissue surrounding the simulation volume, zero oxygen and tracer flows into the volume were set as external boundary conditions. All parameters related to this model have been described in previously published studies, and the references and values applied here are summarized in Table 2.

2.2. Parametric sensitivity study for the FMISO dynamics

2.2.1. VF and vascular architecture

Vascular architectures were considered as arrays of vessels modelled as circular cylinder with 10 μm radius. Tumour samples of $500 \times 500 \times 500\mu m^3$ were simulated employing VFs of 1% and 3%. Two types of vascular architectures were analysed, similar to those simulated in previously published studies [12,23]: parallel and orthogonal vessels (parallel to the x, y, or z axis). In both cases, the vessels covered the whole length of the volume. The spatial vessel distribution and direction of the vessels in 3D were generated randomly using a uniform probability distribution. For each combination of VF (1% or 3%) and vascular architecture type, ten different tumour samples were generated.

2.2.2. Experimental and artificial AIFs

The impact of the AIF on the FMISO uptake was analysed using the parallel vessel architecture with VFs 1% and 3%. Experimental patient AIFs were modelled by double-exponential functions (Eq. (5)), fitted to the mean AIF as presented by Wack *et al.* [21], as well as to the upper and lower 95%-confidence limits (CL). Two additional artificial AIFs were generated having the same area under the curve as the mean experimental AIF, during the first 120 min, but showing a slowly decreasing or a flat shape, respectively. The AIFs are shown in Fig. 1 and the corresponding fitting parameters are presented in Table 1.

2.2.3. Parameters related to the FMISO uptake

The sensitivity study for the tracer uptake was performed using the parallel vessel architecture with VFs of 1% and 3%. Parameter values were varied using the minimum, maximum and mean values of the intervals shown in Table 2. The effects of parameter variation on the tracer binding C_b as a function of P, as well as the TAC shape, were studied. For this, the TAC was calculated according to:

$$\mathrm{TAC}(t) = C_f(t) + C_b(t) + \mathrm{AIF}(t)\bullet\mathrm{VF} \tag{6}$$

2.3. Impact on clinically-relevant PET-parameters for hypoxia assessment

Based on the parametric sensitivity analysis, those input parameters with greater impact on the simulated FMISO uptake were selected to study the resulting variability of the clinically-employed parameters,

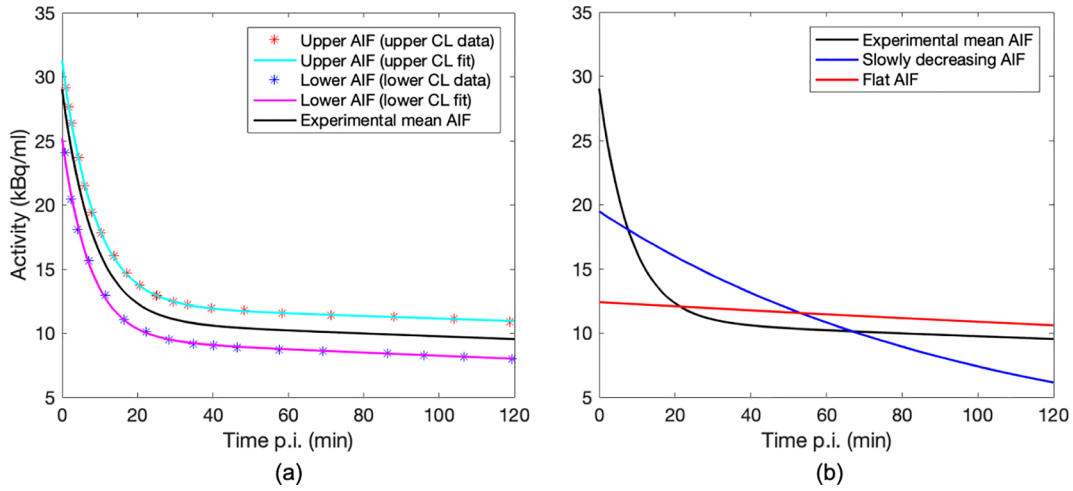

Fig. 1. Experimental AIFs from Wack *et al.* [21] (a) and artificial AIFs (red and blue curves in b).

Table 1
Fit parameters according to Equation (5), describing the AIFs used in this study.

Fitting parameters for AIFs	A_1(kBq/ml)	A_2(kBq/ml)	τ_1 (s^{-1})	τ_2(s^{-1})
Experimental AIFs [21]				
Upper AIF (upper CL)	19.13	12.16	1.93×10^{-3}	1.47×10^{-5}
Mean AIF	18.11	10.93	2.00×10^{-3}	1.90×10^{-5}
Lower AIF (lower CL)	15.64	15.64	2.24×10^{-3}	2.48×10^{-5}
Artificial AIFs				
Slowly decreasing AIF	11.03	8.44	2.00×10^{-4}	1.21×10^{-4}
Flat AIF	8.40	4.00	2.00×10^{-5}	2.59×10^{-5}

Table 2
Parameter values (in bold) used to simulate the spatiotemporal oxygen and FMISO distributions.

Parameter	Symbol	Value
Oxygen distribution		
Intravessel P in tumours	P_{iv}	40mmHg [17]
Capillary permeability to oxygen	L_{O_2}	4.1×10^{-4}ms^{-1} [17]
Oxygen diffusion coefficient	D_{o_2}	2×10^{-9}m^{2}s^{-1} [17]
Maximum oxygen consumption rate	g_{max}	15mmHg s^{-1} [17]
Michaelis-Menten coefficient of oxygen consumption	P_0	2.0mmHg [17]
FMISO dynamics		
Capillary permeability to FMISO	L_T	(**2.4** – 9.4) $\times 10^{-5}$ms^{-1} [16]
FMISO diffusion coefficient	D_T	(**5.5** – 7.9) $\times 10^{-11}$m^{2}s^{-1} [21,25]
P inhibiting binding by 50% of its maximum	P_1	(0.8 – **1.5**)mmHg [26]
Maximum binding rate	K_{max}	(**1.7** – 4.5) $\times 10^{-4}$s^{-1} [17,23]
P inducing 50% necrosis	P_2	(**0.1** – 1.0)mmHg [17,27]
Viable-necrotic tissue transition steepness factor	k	(**0.3** – 1.0) [17]

TBR and FHP [19], at 120 min post injection (p.i.):

$$\text{TBR}(120\text{ min p.i.}) = \frac{\text{TAC (120 min p.i.)}}{\text{AIF (120 min p.i.)}} \tag{7}$$

$$\text{FHP}(120\text{ min p.i.}) = \frac{\text{TAC (120 min p.i.)}}{\bar{\text{TAC}}\big|_{0\text{ min}}^{15\text{ min}}} \tag{8}$$

2.4. Simulations software tools and analysis of results

Vascular architectures were generated in *Gmsh* [28] and used as input to solve all PDEs via the finite element method with *FEniCS* [29], both available as open-source softwares. Since the tracer distribution depends on the stationary oxygen distribution, Eq. (1) was solved first. The P distribution was saved and used as input to solve equations Eqs. (2a) and (2b). The time-dependent tracer distribution was evaluated between 0 and 120 min p.i.. Results were analysed by oxygen histograms, plots of C_b as a function of P, and TACs. The behaviour of TBR and FHP with respect to the hypoxic fraction (HF, fractional volume with $P < 5$ mmHg) was studied. All plots were generated using MATLAB R2016b (The Mathworks Inc., MA), while the visualization of P and tracer distributions was performed using the open-source software *Paraview* [30].

3. Results

Fig. 2 shows the simulated distributions of P and C_b for a sample architecture with parallel vessels and VF 3%. Increased FMISO binding can be seen at large distances from the vessels.

3.1. Parametric sensitivity study for the FMISO dynamics

3.1.1. VF and vascular architecture

Fig. 3 shows the oxygen histograms and TACs simulated for the parallel and orthogonal vessel architectures, with VFs 1% and 3%. The better oxygenation achieved for the 3% VF is reflected by the oxygen histogram exhibiting reduced HF. The largest variability between the different simulated samples was found at the lowest P values. Increasing the VF from 1% to 3% led to increased peak in the TAC at early time points (from 0 to 20 min p.i.) and decreased tracer uptake at large p.i. times. A larger TAC variability was found for VF 1%. No significant differences in oxygenation and TACs were found when comparing parallel and orthogonal vessel architectures for different VF.

3.1.2. Experimental and artificial AIFs

Fig. 4 shows the TACs for the parallel vessel architecture with VF 1% simulated using different AIFs as input. The vertical shifts between the three experimental AIFs (Fig. 4a) led to similar shifts of the TACs that were larger than the sampling variability. For the artificial AIFs, the TAC shape changed drastically (Fig. 4b). For the slowly decreasing AIF, the TAC peaked later than for the mean experimental AIF. In contrast, the TAC simulated with the flat AIF did not show any initial peak, but rather a continuously increasing binding with time.

3.1.3. Parameters related to the FMISO uptake

Fig. 5 shows C_b as a function of P for different parameter settings in the FMISO dynamics model. The shape of $C_b(P)$ was basically the same

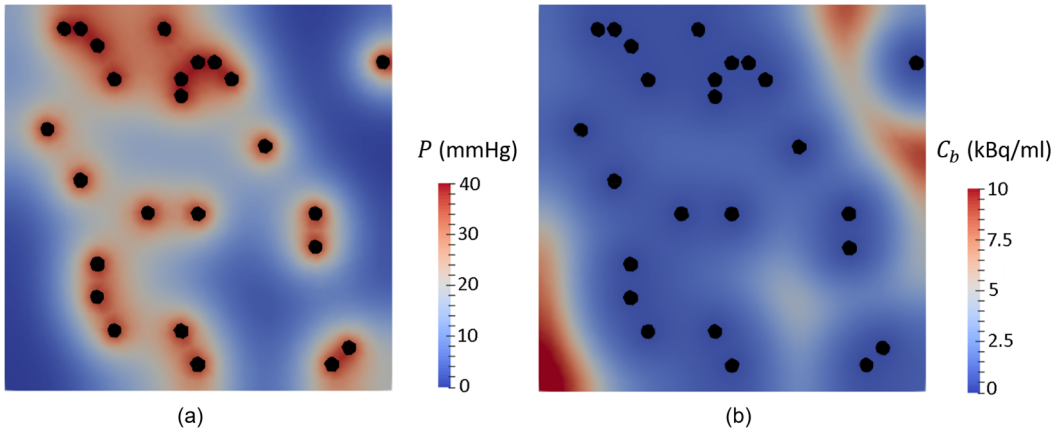

Fig. 2. Example of simulated P (a) and C_b distributions, 120 min p.i., for a sample of the parallel vessels (black circles) architecture with VF 3%. Distributions are shown for the central plane of the simulated tumour volume.

for all settings: the binding increased with increasing P, reached a maximum at around 2 mmHg and decreased after. Essentially, no variation was observed for varying L_T and D_T values. Increasing P_1 and K_{max} separately led to an increased binding, for $P > 0.1$ mmHg and for all P values, respectively. Increasing separately the value of P_2 and k led to a decreased binding for $P < 2$ mmHg and a shifting of the binding maximum towards larger P values.

Fig. 6 displays the TACs for all parameter settings. Increasing VF from 1% to 3% altered significantly the height of the peak at early p.i. times, and the tracer accumulation at late p.i. times. As shown for the

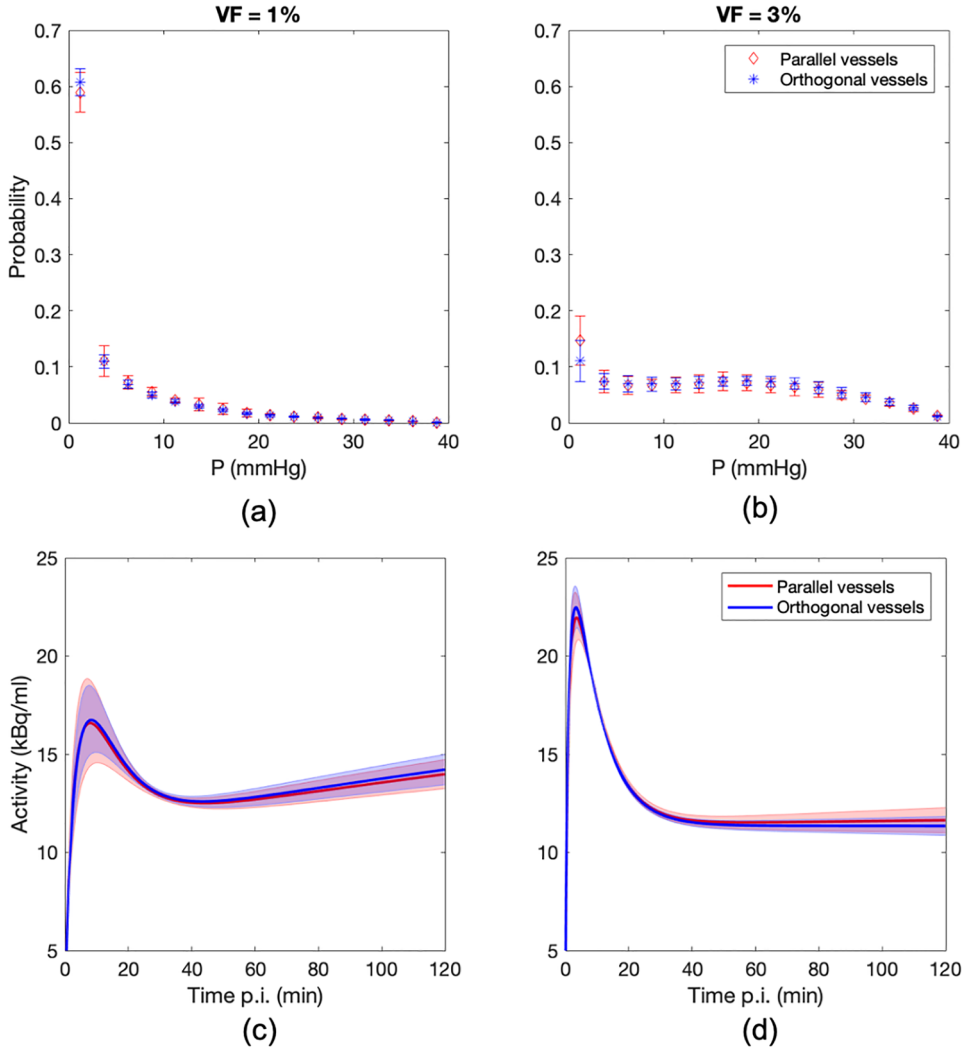

Fig. 3. Simulated probability distributions for P (a, b) and TACs (c, d) for parallel (red) and orthogonal (blue) vessel distributions, using VFs of 1% (a, c) and 3% (b, d). Errors bars represent single standard deviations over the ten simulated samples. TAC shaded regions represent the 95% confidence interval for the ten simulated samples.

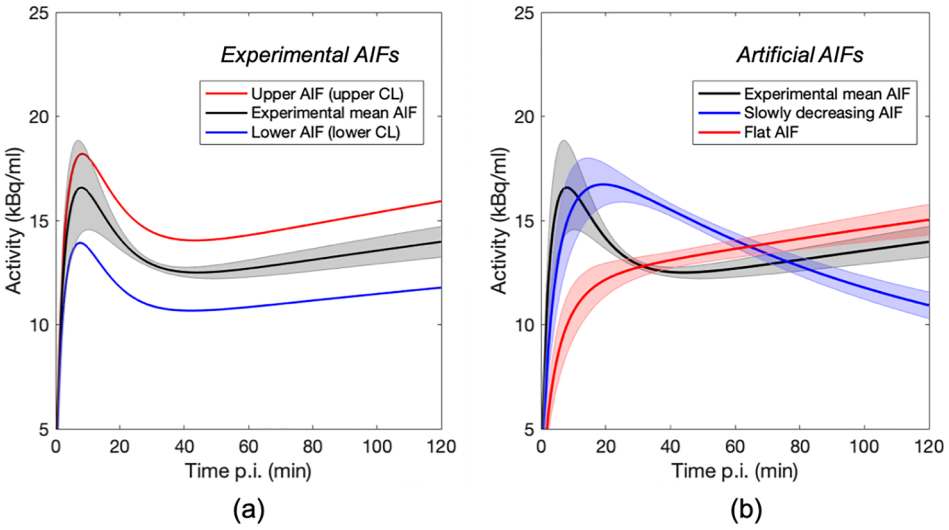

Fig. 4. Simulated TACs for experimental AIFs from Wack *et al.* [21] (a) and for artificial AIFs (blue and red curves in b) for the parallel vessel architecture and VF 1%. Shaded regions show the 95% confidence interval for the ten simulated samples. For better visibility, confidence intervals are shown only for the mean AIF in (a).

central parameter settings (Table 2) by the shaded regions, the TAC was sensitive to the sampling variability, and the TAC variation was larger for VF 1% than for 3%. Regarding the different parameter settings, TACs did not differ significantly for varying L_T, and only small differences in the peak were found for D_T. Also, for P_1 only minor differences in the uptake were seen at large p.i. times. The largest sensitivity of the TAC was found for variations of K_{max}, which exhibited identical peak heights but markedly different tracer uptakes at large p.i. times. Varying the values of P_2 and k did not change the peak height but led to changes of the late uptake, of the same magnitude as the sample variation.

3.2. Impact on clinically-relevant parameters for PET-based hypoxia assessment

Based on Figs. 4–6, the most relevant parameters influencing the FMISO uptake were K_{max} and the AIF. For different settings of these two parameters, TBRs and FHPs were calculated for VFs 1% and 3%, and the obtained values are shown Table 3.

For the mean AIF, increased K_{max} led to increased TBR, and this trend was more pronounced for VF 1%. For the same value of K_{max}, larger TBR was obtained for smaller VF, and therefore in this case TBR allowed discriminating between the two VF and the related HF. However, a comparable TBR was obtained for $K_{max} = 1.7 \times 10^{-4}$1/s at VF 1% and for $K_{max} = 4.5 \times 10^{-4}$1/s at VF 3%.

Only small differences in TBRs were obtained for the flat AIFs at VF 1% and 3%. In contrast, TBR-differences were markedly larger for the slowly decreasing AIF. Assuming the same AIF, differentiation of VF based on TBR-values was possible.

For the mean AIF, increased K_{max} led to increased FHP and lower FHPs were obtained at VF 3% for all K_{max} values, in comparison to VF 1%. Therefore, FHP also allowed discriminating between the two VF.

Compared to the mean AIF at the same value of K_{max}, FHP was larger for the flat than for the slowly decreasing AIF. For the same AIF, FHP allowed discriminating different VF and HF, however, FHP for the flat AIF at VF 3% was larger than that for the mean and slowly decreasing AIF at VF 1%.

4. Discussion

4.1. Parametric sensitivity study for the FMISO dynamics

In accordance with previous studies [12,23], very similar oxygen distributions were found for architectures with parallel and orthogonal vessels, as long as the same VF and the same degree of heterogeneity in the vessel distribution were used. This is in accordance with the study by Warren and Partridge [23], who analysed vascular architectures with isotropic vessel orientations and showed similar oxygen distributions. This leads to the conclusion that oxygen distributions for these three types of vascular architectures are the same on a macroscopic level, for identical VF and degree of heterogeneity in the vessel distribution. We therefore restricted further analysis to the parallel vessel architecture.

While high P values may result from a small distance from a single vessel or moderate distances to multiple vessels, low P values depend critically on the largest distance to the nearest vessels, which is in the order of the oxygen diffusion radius. Low P values are therefore more dependent on the individual vessel position and thus exhibit larger variations in the sampling experiments. The impact of the VF can be clearly seen in the TACs. While the TAC at VF 3% exhibits a prominent initial peak, which indicates a good perfusion, the TAC at VF 1% resulted in a reduced peak with an increased uptake at large p.i. times, indicating a reduced perfusion with increased hypoxia.

TACs clearly reflect differences in VF, and it also depends critically on the AIF (Figs. 1 and 4), as previously shown by Wack *et al.* [21]. For different investigated AIFs, the TAC variations were larger than sampling variability. In principle, the AIF can be measured simultaneously with the TAC and may then be used to remove or reduce the dependence of the measured parameters on the AIF. Examples for such parameters are the TBR, where TACs are normalized to AIF-values, or physiological parameters, determined in more advanced pharmacokinetic analyses. In real measurements, however, the AIF is typically measured in the heart or in a large artery proximal to the tumour to avoid partial volume effects. Depending on how the tumour is connected to the vascular system, an initially sharply peaked AIF will spread and the actual AIF in the tumour may be less sharp or even flat as simulated in our study by the “slowly decreasing” or “flat” AIF. Thus, even if the measured parameters are corrected for the impact of the AIF, it may still include some uncertainty resulting from the fact that the measured rather than the actual AIF of the tumour has been used. The strong dependence of the TAC on the AIF may also explain the very different TAC shapes observed by Mena-Romano *et al.* [31] in three different rat prostate tumour sublines.

Besides VF and AIF, the highest sensitivity of the TACs was found for the maximum binding rate K_{max}. While the exact value of this parameter is unknown, it is primarily a chemical reaction constant, which

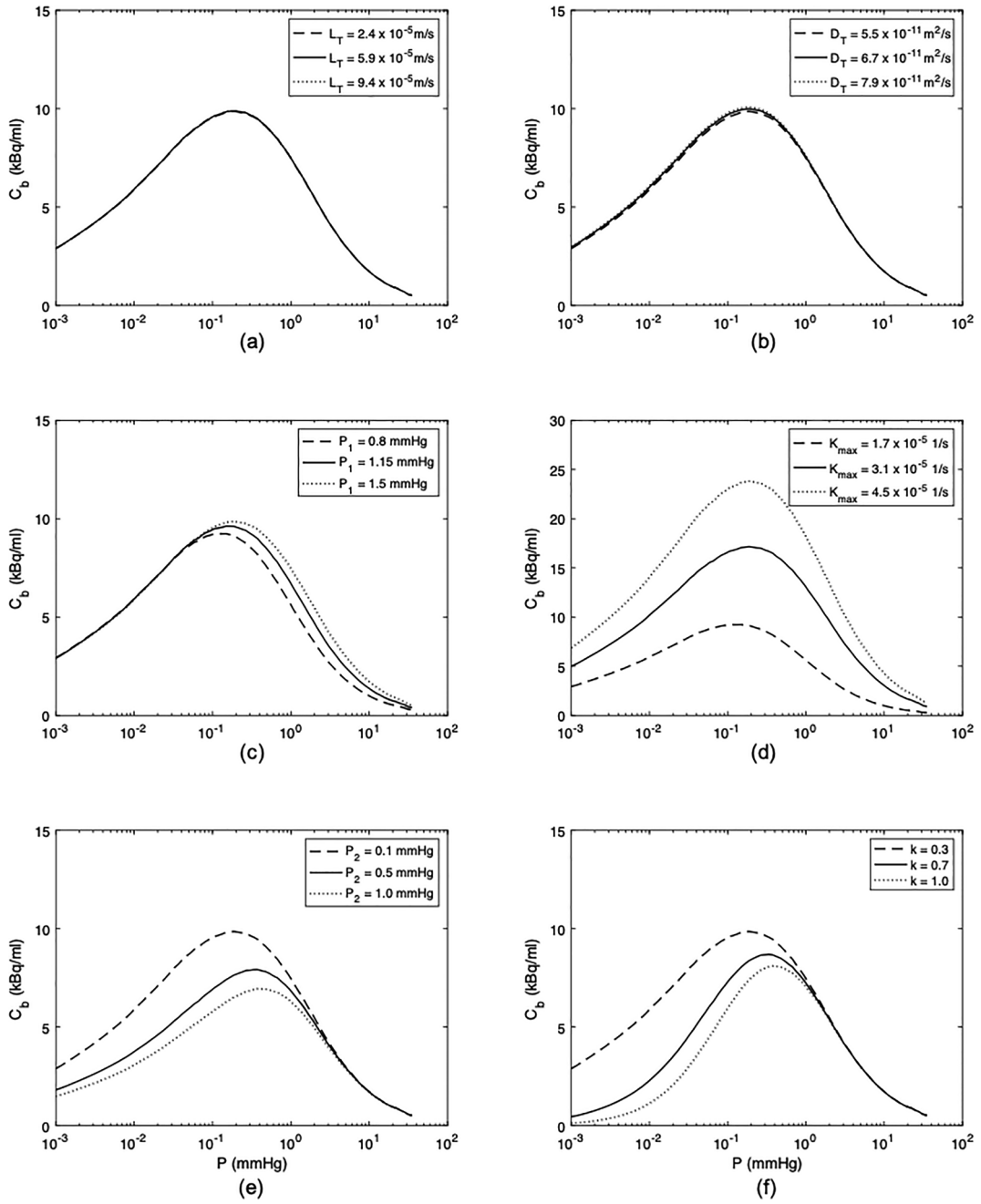

Fig. 5. Simulated FMISO binding concentration C_b as a function of P at 120 min p.i., for all parameters related to the FMISO dynamics model using the experimental mean AIF: FMISO capillary permeability L_T (a), FMISO diffusion coefficient D_T (b), P_1 indicating the value of P for 50% binding (c), maximum binding rate K_{max} (d), P_2 indicating the value of P for 50% necrosis (e), and transition steepness factor for necrosis k (f). Simulations were performed for the parallel vessel architecture and VF 1% using the reference parameter settings and in each plot, the denoted parameter was varied within the ranges shown in Table 2.

should not differ between different cell lines although it cannot be ruled-out that there is an additional dependence on the tracer uptake into the cell and the nucleus.

The model used to simulate the FMISO dynamics showed the complex behaviour of tracer binding, exhibiting a reduced binding for both well-oxygenated and very poorly oxygenated regions, which are assumed to become necrotic (Fig. 5). While it is undoubted that severe hypoxia can lead to necrosis and that FMISO will not bind to necrotic regions, the oxygen level leading to necrosis as well as the underlying time scale is unknown and may vary between cell lines as they may adapt differently to the hypoxic environment. With this respect, the modelling of the uptake in necrotic regions by the function $F_2(P)$ has to be considered as a heuristic approach, which may be questioned. In contrast, the uptake function in hypoxic but viable tissue regions, $F_1(P)$ appears more reliable as the underlying mechanism is better understood. In addition, only minor changes of the uptake was found for variations of the related parameter P_1.

In contrast to the parameters describing the tracer uptake, tracer binding (Fig. 5) and TAC shape (Fig. 6) turned out to be essentially independent of the permeability L_T and the diffusion coefficient D_T. As shown by Kelly and Brady [16], relevant TAC changes may be observed only when these parameters are varied by an order of magnitude.

4.2. Reliability of clinically-relevant PET-parameters

PET-based hypoxia assessment is often performed using parameters

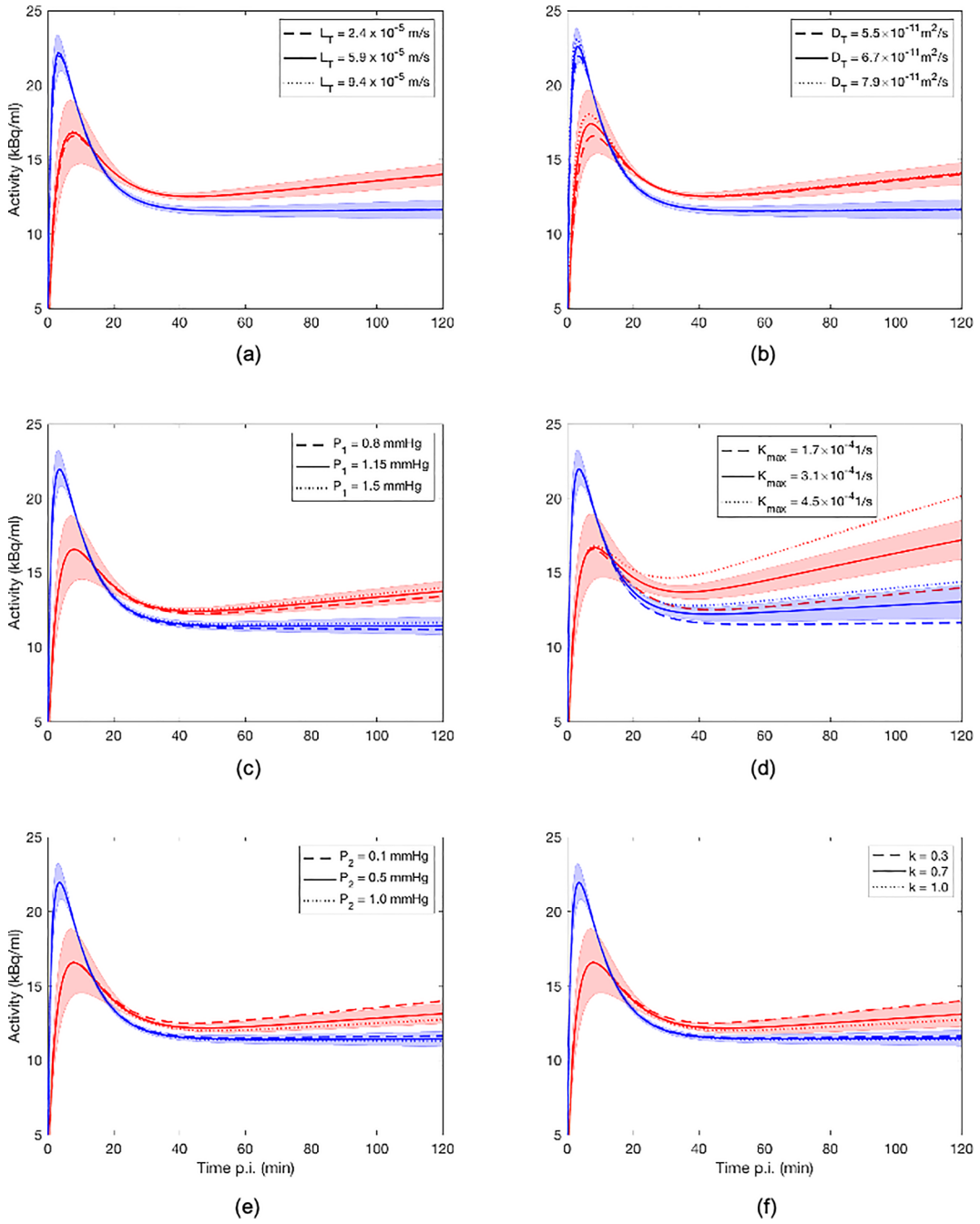

Fig. 6. TACs simulated with the experimental mean AIF and different parameter settings of the FMISO dynamics model, for the parallel vessel architecture with VFs of 1% (red curves) and 3% (blue curves): FMISO capillary permeability L_T (a), FMISO diffusion coefficient D_T (b), P_1 indicating the value of P for 50% binding (c), maximum binding rate K_{max} (d), P_2 indicating the value of P for 50% necrosis (e), and transition steepness factor for necrosis k (f). Simulations were performed for the reference parameter settings and in each plot, the denoted parameter was varied within the ranges shown in Table 2. Each TAC represents an average over ten samples shown in solid, dashed and dotted lines. Shaded regions represent the 95% confidence interval of the simulations performed with the central parameter setting (solid line).

such as tissue-to-blood ratios, tissue-to-muscle ratios, or standardized uptakes values (SUV), which are uptake measurements, normalized to that of a reference volume or to the injected activity per mass and which can be used without additional use of detailed pharmacokinetic models. TBR is determined in a region of interest at a certain p.i. time and is normalized to the activity in the blood (Eq. (7)). FHP was suggested by Mönnich *et al.* [19] as a "measure of hypoxia-related tracer retention that is normalized by a simple measure of perfusion" (Eq. (8)) and it was found that FHP allowed assessing the median P with higher accuracy than with a simple measurement at 4 h p.i.

As shown in Table 3, larger or comparable TBRs may be obtained for VF 3% than for 1%, for different K_{max} values. Therefore, if K_{max} varies within the tumour, discriminating between hypoxic and non-hypoxic tissues may become difficult. In contrast, the parameter FHP can still discriminate these conditions. On the other hand, if K_{max} is considered only as a chemical reaction constant, independent of the transport capabilities of the cell membranes, either TBR or FHP may be used to distinguish different degrees of oxygenation.

Regarding the dependence on the AIF, the parameter FHP could not always distinguish different VF, since this metric depends on the

Table 3
TBR and FHP (mean ± standard deviation) for different maximum binding rates K_{max} and AIFs, for VFs 1% and 3% (and corresponding HFs, mean ± standard deviation). Standard deviations were calculated for the ten simulated samples.

AIF	Flat	Slowly decr.	Mean	Mean	Mean
K_{max} [$\times 10^{-4}$ 1/s]	1.7	1.7	1.7	3.1	4.5
TBR					
VF = 1%*	1.42 ± 0.04	1.78 ± 0.05	1.47 ± 0.04	1.81 ± 0.07	2.12 ± 0.10
VF = 3%+	1.20 ± 0.03	1.34 ± 0.06	1.22 ± 0.03	1.37 ± 0.06	1.51 ± 0.08
FHP					
VF = 1%*	1.67 ± 0.08	0.81 ± 0.04	0.94 ± 0.04	1.14 ± 0.04	1.33 ± 0.05
VF = 3%+	1.10 ± 0.08	0.48 ± 0.04	0.63 ± 0.02	0.70 ± 0.04	0.77 ± 0.05

* HF = 70.3% ± 2.7%.
\+ HF = 22.5% ± 5.4%.

relation between late and early values of the TAC, which changes drastically between the different AIFs. Especially for the flat AIF, the lack of an initial peak led to markedly increased FHP-values. This complicates especially the inter-individual comparison of FHP-values if the tumours have significantly different AIFs. The parameter TBR, on the other hand, allowed distinguishing the different VF independently of the actual AIF. However, inter-individual variations of the AIF will lead to variation of TBR, which introduces additional uncertainty in the comparison of TBR-values between different tumours. This problem persists for both parameters TBR and FHP as long as the measured AIF does not truly reflect the actual AIF in the tumour.

5. Conclusion

This study implemented a model for hypoxia-PET radiotracer dynamics and performed a parametric sensitivity study to gain insight in the relationship between ^{18}F-fluoromisonidazole (FMISO) transport processes and time-activity curves (TACs), tissue-to-blood ratios (TBRs) and the hypoxia-perfusion compound parameter FHP. The input parameters considered were vascular architecture, vascular fraction (VF), arterial input function (AIF) and parameters related to the FMISO dynamics. The most sensitive parameters were the AIF and the maximum binding rate (K_{max}). TBR allowed discriminating VF for different AIF, and FHP for different K_{max}, but neither TBR nor FHP were unbiased in all cases. This bias may especially occur in the comparison of TBR- or FHP-values between different tumours, where the relation between measured and actual AIF may vary. Thus, these parameters represent only surrogates rather than absolute measurements of hypoxia in tumours.

Funding sources

I.P-C acknowledges travel grants as well as funding for scholarships for temporary exchanges between the Pontificia Universidad Católica de Chile (UC) and the German Cancer Research Center (DKFZ) received from the German Academic Exchange Service (DAAD). D.N. was supported by the grant CONICYT Doctorado Nacional (project 21151353). I.E and A. G-A acknowledge the support of FONDECYT 111505601 and 11170575, respectively. Funding sources were not involved in the study design; collection, analysis and interpretation of data; writing of the report; or in the decision to submit the article for publication.

Declaration of Competing Interest

The authors declare that they have no known competing financial interests or personal relationships that could have appeared to influence the work reported in this paper.

References

[1] Nordsmark M, Overgaard M, Overgaard J. Pretreatment oxygenation predicts radiation response in advanced squamous cell carcinoma of the head and neck. Radiother Oncol 1996;41:31–9. https://doi.org/10.1016/S0167-8140(96)91811-3.
[2] Vaupel P. Tumor microenvironmental physiology and its implications for radiation oncology. Semin Radiat Oncol 2004;14:198–206. https://doi.org/10.1016/j.semradonc.2004.04.008.
[3] Li F, Joergensen JT, Hansen AE, Kjaer A. Kinetic modeling in PET imaging of hypoxia. Am J Nucl Med Mol Imaging 2014;4:490–506. https://doi.org/10.1056/NEJMra1313875.
[4] Peeters SGJA, Zegers CML, Lieuwes NG, Van Elmpt W, Eriksson J, Van Dongen GAMS, et al. A comparative study of the hypoxia PET tracers [18F]HX4, [18F]FAZA, and [18F]FMISO in a preclinical tumor model. Int J Radiat Oncol Biol Phys 2015;91:351–9. https://doi.org/10.1016/j.ijrobp.2014.09.045.
[5] Zips D, Zöphel K, Abolmaali N, Perrin R, Abramyuk A, Haase R, et al. Exploratory prospective trial of hypoxia-specific PET imaging during radiochemotherapy in patients with locally advanced head-and-neck cancer. Radiother Oncol 2012;105:21–8. https://doi.org/10.1016/j.radonc.2012.08.019.
[6] Welz S, Mönnich D, Pfannenberg C, Nikolaou K, Reimold M, La Fougère C, et al. Prognostic value of dynamic hypoxia PET in head and neck cancer: results from a planned interim analysis of a randomized phase II hypoxia-image guided dose escalation trial. Radiother Oncol 2017;124:526–32. https://doi.org/10.1016/j.radonc.2017.04.004.
[7] Mortensen LS, Johansen J, Kallehauge J, Primdahl H, Busk M, Lassen P, et al. FAZA PET/CT hypoxia imaging in patients with squamous cell carcinoma of the head and neck treated with radiotherapy: results from the DAHANCA 24 trial. Radiother Oncol 2012;105:14–20. https://doi.org/10.1016/j.radonc.2012.09.015.
[8] Thorwarth D, Eschmann SM, Paulsen F, Alber M. Hypoxia dose painting by numbers: a planning study. Int J Radiat Oncol Biol Phys 2007;68:291–300. https://doi.org/10.1016/j.ijrobp.2006.11.061.
[9] Thorwarth D, Geets X, Paiusco M. Physical radiotherapy treatment planning based on functional PET/CT data. Radiother Oncol 2010;96:317–24. https://doi.org/10.1016/j.radonc.2010.07.012.
[10] Grimes DR, Warren DR, Warren S. Hypoxia imaging and radiotherapy: bridging the resolution gap. Br J Radiol 2017;90. https://doi.org/10.1259/bjr.20160939.
[11] Daşu A, Toma-Daşu I, Karlsson M. Theoretical simulation of tumour oxygenation and results from acute and chronic hypoxia. Phys Med Biol 2003;48:2829–42. https://doi.org/10.1088/0031-9155/48/17/307.
[12] Espinoza I, Peschke P, Karger CP. A model to simulate the oxygen distribution in hypoxic tumors for different vascular architectures. Med Phys 2013;40:1–12. https://doi.org/10.1118/1.4812431.
[13] Toma-Dasu I, Dasu A. Modelling tumour oxygenation, reoxygenation and implications on treatment outcome. Comput Math Methods Med 2013;2013. https://doi.org/10.1155/2013/141087.
[14] Casciari JJ, Rasey JS. Determination of the radiobiologically hypoxic fraction in multicellular spheroids from data on the uptake of [3 H]fluoromisonidazole. Radiat Res 1995;141:28. https://doi.org/10.2307/3579086.
[15] Thorwarth D, Eschmann SM, Paulsen F, Alber M. A kinetic model for dynamic [18F]-Fmiso PET data to analyse tumour hypoxia. Phys Med Biol 2005;50:2209–24. https://doi.org/10.1088/0031-9155/50/10/002.
[16] Kelly CJ, Brady M. A model to simulate tumour oxygenation and dynamic [18F]-Fmiso PET data. Phys Med Biol 2006;51:5859–73. https://doi.org/10.1088/0031-9155/51/22/009.
[17] Mönnich D, Troost EGC, Kaanders JHAM, Oyen WJG, Alber M, Thorwarth D. Modelling and simulation of [18F]fluoromisonidazole dynamics based on histology-derived microvessel maps. Phys Med Biol 2011;56:2045–57. https://doi.org/10.1088/0031-9155/56/7/009.
[18] Mönnich D, Troost EGC, Kaanders JHAM, Oyen WJG, Alber M, Thorwarth D. Modelling and simulation of the influence of acute and chronic hypoxia on [18F] fluoromisonidazole PET imaging. Phys Med Biol 2012;57:1675–84. https://doi.org/10.1088/0031-9155/57/6/1675.
[19] Mönnich D, Troost EGC, Kaanders JHAM, Oyen WJG, Alber M, Zips D, et al. Correlation between tumor oxygenation and 18F-fluoromisonidazole PET data

simulated based on microvessel images. Acta Oncol (Madr) 2013;52:1308–13. https://doi.org/10.3109/0284186X.2013.812796.
[20] Skeldon AC, Chaffey G, Lloyd DJB, Mohan V, Bradley DA, Nisbet A. Modelling and detecting tumour oxygenation levels. PLoS One 2012;7:1–17. https://doi.org/10.1371/journal.pone.0038597.
[21] Wack LJ, Mönnich D, Van Elmpt W, Zegers CML, Troost EGC, Zips D, et al. Comparison of [18F]-FMISO, [18F]-FAZA and [18F]-HX4 for PET imaging of hypoxia - a simulation study. Acta Oncol (Madr) 2015;54:1370–7. https://doi.org/10.3109/0284186X.2015.1067721.
[22] Wack LJ, Monnich D, Yaromina A, Zips D, Baumann M, Thorwarth D. Correlation of FMISO simulations with pimonidazole-stained tumor xenografts: a question of O2 consumption? Med Phys 2016;43:4113. https://doi.org/10.1118/1.4951728.
[23] Warren DR, Partridge M. The role of necrosis, acute hypoxia and chronic hypoxia in 18F-FMISO PET image contrast: a computational modelling study. Phys Med Biol 2016;61:8596–624. https://doi.org/10.1088/1361-6560/61/24/8596.
[24] Secomb TW, Hsu R, Park EYH, Dewhirst MW. Green's function methods for analysis of oxygen delivery to tissue by microvascular networks. Ann Biomed Eng 2004;32:1519–29. https://doi.org/10.1114/B:ABME.0000049036.08817.44.
[25] Cowan D, Hicks K, Wilson W. Multicellular membranes as an in vitro model for extravascular diffusion in tumours. Br J Cancer 1996;74:28–31.
[26] Rasey JS, Koh WJ, Grierson JR, Grunbaum Z, Krohn KA. Radiolabeled fluoromisonidazole as an imaging agent for tumor hypoxia. Int J Radiat Oncol Biol Phys 1989;17:985–91. https://doi.org/10.1016/0360-3016(89)90146-6.
[27] Harriss-Phillips WM, Bezak E, Yeoh E. The HYP-RT hypoxic tumour radiotherapy algorithm and accelerated repopulation dose per fraction study. Comput Math Methods Med 2012;2012. https://doi.org/10.1155/2012/363564.
[28] Geuzaine C, Remacle JJ. Gmsh: a three-dimensional finite element mesh generator with built-in pre- and post-processing facilities, (2019). http://gmsh.info/ [Accessed February 20, 2019].
[29] Alnæ MS, Blechta J, Hake J, Johansson A, Kehlet B, Richardson C, Ring J, Rognes ME, Wells GN. The FEniCS Project Version 1.5, Arch. Numer. Softw. 3 (2015) 9–23. https://journals.ub.uni-heidelberg.de/index.php/ans/article/view/20553/20092 [Accessed July 19, 2019].
[30] Kitware, ParaView, (2017). https://www.paraview.org/ [Accessed February 20, 2019].
[31] Mena-Romano P, Cheng C, Glowa C, Peschke P, Pan L, Haberkorn U, et al. Measurement of hypoxia-related parameters in three sublines of a rat prostate carcinoma using dynamic 18F-FMISO-PET-CT and quantitative histology. Am J Nucl Med Mol Imaging 2015;5:348–62. https://doi.org/10.1016/S0167-8140(15)31924-1.